引用格式：GU Kai, SUN Fanxi, TAO Guanyu. Manipulation of Surface Plasmon Polariton Vortices via Positive Elliptically Polarized Light and Geometric Phase[J]. Acta Photonica Sinica, 2026, 55(1):0124001
顾凯,孙凡茜,陶冠宇.基于正椭偏光和几何相位调控表面等离激元涡旋[J].光子学报,2026,55(1):0124001

基于正椭偏光和几何相位调控表面等离激元涡旋

顾凯,孙凡茜,陶冠宇
(宿迁学院 数理学院,宿迁 223800)

摘　要:现有基于正椭偏光的等离激元涡旋透镜,在激发具有高阶拓扑荷涡旋时均需引入传输相位,限制了其小型化应用。提出一种基于几何相位的新型等离激元涡旋透镜,该结构由排列于圆形轮廓上的组合元原子构成,每个元原子集成四个矩形狭缝。研究结果表明,该设计仅利用几何相位即可在正椭偏光激励下激发任意阶表面等离激元涡旋,与传统依赖传输相位的方案相比提升了器件的紧凑性,为光子器件的微型化设计与集成化应用提供了可行路径。此外,通过调控元原子内狭缝的旋转角度,可实现器件对包括正椭偏光旋向与振幅比在内的偏振敏感性调控,拓展了该器件在光开关与生物传感等领域的应用前景。

关键词:表面等离激元;涡旋;拓扑荷;正椭偏光;几何相位;偏振敏感性
中图分类号:O436　　**文献标识码**:A　　**doi**:10.3788/gzxb20265501.0124001

0　引言

表面等离激元(Surface Plasmon Polariton, SPP)因其独特的短波长、强近场局域与增强效应,已被广泛应用于亚波长光刻[1,2]、超分辨成像[3,4]、激光物理[5-7]、光子集成[8-11]、生化传感[12-18]及表面增强拉曼散射[19-22]等领域。进一步地,将光学涡旋的轨道角动量(Orbital Angular Momentum, OAM)耦合至SPP,可在金属表面形成具有均匀环状强度分布和连续螺旋相位的SPP涡旋场。此类携带OAM的SPP涡旋场在粒子操控[23,24]、生化分析[25,26]、光场探测[27]和高安全性加密[28]等领域展现出重要应用价值。

近年来,用于激发SPP涡旋的等离激元涡旋透镜(Plasmonic Vortex Lens, PVL)研究不断深入,其激发光源已从需携带OAM的复杂矢量光场简化为圆偏振光或线偏振光的标量光场[29-32]。正椭偏光作为标量光场的关键偏振态之一,虽已被用作PVL的激发源,但现有方案产生SPP涡旋场的强度普遍依赖于入射正椭偏光的旋向及振幅比[33-38],制约了SPP涡旋及PVL器件的应用灵活性。为拓展PVL的应用范围,研究者设计了一种利用双矩形狭缝排列在螺旋轮廓上的PVL,在正椭偏光入射的情况下,能产生对入射正椭偏光的振幅比与旋向不敏感的SPP涡旋[39]。然而,此类能够生成任意阶SPP涡旋的PVL必须依赖传输相位调控,即必须采用螺旋轮廓设计。在螺旋结构中,不同位置处的元原子所激发的SPP波,在传播至聚焦中心时的光程存在差异,导致其衰减程度不同,难以实现理想的均匀环状强度分布。该不均匀性在激发短波长SPP涡旋时尤为显著,因为SPP的传播衰减随波长减小而非线性增强。此外,螺旋轮廓固有的空间角依赖性导致其末端半径大于始端半径,阻碍了器件的微型化设计,这一问题在长波长器件中更为突出。

针对上述挑战,本文提出一种基于几何相位的新型PVL设计。该透镜由排列于圆形轮廓上的组合元原子构成,每个组合元原子包含四个矩形狭缝。通过系统性调控元原子内狭缝的旋转角度,该PVL不仅能在正椭偏光激励下产生对入射正椭偏光的振幅比与旋向敏感或不敏感的SPP涡旋,还能灵活调控SPP涡旋的拓扑荷,拓展了器件在光开关、生物检测等领域的应用前景[40-41]。由于仅采用单一形状和尺寸的狭缝结构,且仅基于几何相位进行设计,避免了传输相位的引入,显著简化了器件工艺流程,并有效提升了器件的紧凑性,为光子器件的微型化设计与集成化应用提供了解决方案。

基金项目:宿迁市科技计划(K202536),宿迁学院人才引进科研启动基金(2025XRC006)
第一作者(通讯作者):顾凯, gk0730@squ.edu.cn
收稿日期:2025-07-20;**录用日期**:2025-09-15

1 理论模型

首先，在厚度 $h=200\ \mathrm{nm}$ 的金薄膜上，刻蚀出四个长宽比较大、间隔 $D=\lambda_{\mathrm{SPP}}/4$ 的矩形狭缝，构成一个组合元原子。其中，λ_{SPP} 为SPP的波长。随后，将若干此类组合元原子排列于圆形轮廓上，形成PVL。图1为基于组合元原子构建而成的PVL示意图。在PVL结构的右上角，展示了第10个组合元原子内部狭缝的分布细节。组合元原子内的第 s 个矩形狭缝排列在半径为 r_s 的圆形轮廓上（s 分别为1，2，3，4），空间某个位置上的第 m 个组合元原子内每个矩形狭缝长边的法线方向的单位矢量为 $\boldsymbol{t}_{ms}$，其与 x 轴的夹角为 θ_{ms}。

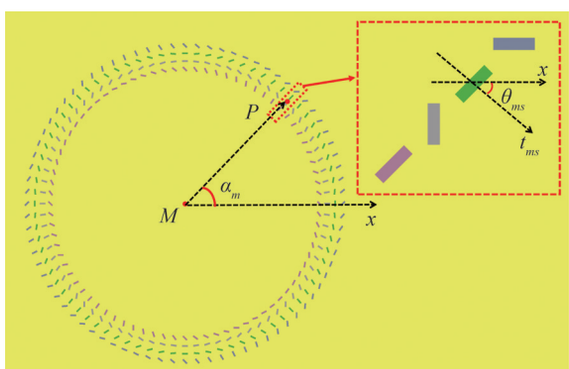


图1 由组合元原子构建的PVL示意图。右上角为第10个组合元原子内狭缝的分布细节

Fig.1 Schematic of the PVL constructed from composite meta-atoms. Top right: detailed view of the slit distribution within the tenth meta-atom

根据单个长宽比较大矩形狭缝激发SPP的规律，可将激发SPP的过程等效为振荡电偶极子的辐射[42-46]。在笛卡尔坐标中，当椭圆偏振光的椭圆长轴和短轴分别与 x 轴和 y 轴平行时，称为正椭圆偏振光[47]。其电场矢量可表示为两个具有特定振幅比和固定 $\pi/2$ 相位差的正交分量的叠加：$\boldsymbol{E}_{\mathrm{in}}=E_{\mathrm{in}}(\cos\varphi,\pm\mathrm{i}\sin\varphi)$。当正椭圆偏振光照射点 P 处的第 m 个组合元原子时（P 点与原点 M 的连线构成矢量 $\boldsymbol{P}$，$\boldsymbol{P}$ 与 x 轴夹角为 α_m），组合元原子内的第 s 个矩形狭缝时，其在原点 M 处激发的SPP场 E_{Mms} 可表示为

$$E_{Mms}=\exp\left(\mathrm{i}k_{\mathrm{SPP}}\rho\right)\left[\left(\boldsymbol{E}_{\mathrm{in}}\cdot\boldsymbol{t}_{ms}\right)\left(\boldsymbol{t}_{ms}\cdot\boldsymbol{P}\right)\right]=\exp\left(\mathrm{i}k_{\mathrm{SPP}}\left(r_2+\frac{(s-2)\lambda_{\mathrm{SPP}}}{4}\right)\right)\left[\left(\cos\varphi\cos\theta_{ms}\pm\mathrm{i}\sin\varphi\sin\theta_{ms}\right)\cos\left(\theta_{ms}-\alpha_m\right)\right] \tag{1}$$

而整体的第 m 个组合元原子在原点 M 处形成的SPP叠加场 E_{Mm} 可以表示为

$$E_{Mm}=\sum_{s=1}^{4}E_{Mms} \tag{2}$$

通过调整组合元原子内各个矩形狭缝的旋转角度，可以形成对正椭偏光旋向和振幅比敏感的PVL1及不敏感的PVL2。

1.1 对正椭偏光旋向和振幅比敏感的PVL1

当第 m 个组合元原子内的四个矩形狭缝的旋转角度满足：$\theta_{m1}=a\alpha_m+b$，$\theta_{m2}=\theta_{m1}+\pi/4$，$\theta_{m3}=a\alpha_m+d$，$\theta_{m4}=\theta_{m3}+\pi/4$，且 $r_2=r$，组成了一个超表面结构PVL1。当正椭偏光入射时，第 m 个组合元原子在 M 点处SPP场可以表示为

$$E_{Mm}=\begin{cases}\sin(b-d)\cos\left(\varphi+\dfrac{\pi}{4}\right)\exp\left[\mathrm{i}\left(k_{\mathrm{SPP}}r+(1-2a)\alpha_m-b-d\right)\right],\Delta=\dfrac{\pi}{2}\\ \sin(b-d)\cos\left(\varphi-\dfrac{\pi}{4}\right)\exp\left[\mathrm{i}\left(k_{\mathrm{SPP}}r+(1-2a)\alpha_m-b-d\right)\right],\Delta=-\dfrac{\pi}{2}\end{cases} \tag{3}$$

忽略SPP在传播过程中的衰减，根据贝塞尔函数性质，可以得到所有组合元原子在原点附近任意一点 $q(\rho,\phi,z)$ 处的SPP叠加场，即

$$E_q=\begin{cases} r\sin(b-d)\cos\left(\varphi+\dfrac{\pi}{4}\right)(-\mathrm{i})^{(1-2a)}\exp\left[\mathrm{i}\left(k_{\mathrm{SPP}}r+(1-2a)\phi-b-d\right)\right]J_{1-2a}(k_{SPP}\rho),\Delta=\dfrac{\pi}{2} \\ r\sin(b-d)\cos\left(\varphi-\dfrac{\pi}{4}\right)(-\mathrm{i})^{(1-2a)}\exp\left[\mathrm{i}\left(k_{\mathrm{SPP}}r+(1-2a)\phi-b-d\right)\right]J_{1-2a}(k_{SPP}\rho),\Delta=-\dfrac{\pi}{2} \end{cases} \tag{4}$$

式中，J_n为n阶第一类贝塞尔函数。从式(4)可以发现，无论入射的正椭圆偏振光的旋向和振幅比如何，最终都能够在PVL1的中央形成拓扑荷为$l=1-2a$的SPP涡旋，并且入射正椭偏光的旋向和振幅比的变化均会导致SPP涡旋场振幅发生改变。因此，PVL1对正椭偏光旋向和振幅比敏感。

1.2 对正椭偏光旋向和振幅比不敏感的PVL2

当第m个组合元原子内的第二个与第四个矩形狭缝的旋转角度满足：$\theta_{m1}=a\alpha_m+b$，$\theta_{m2}=\theta_{m1}+\pi/4$，$\theta_{m3}=c\alpha_m+d$，$\theta_{m4}=\theta_{m3}-\pi/4$，且$r_2=r$时，构成的PVL被定义为PVL2。当正椭偏光入射时，第m个组合元原子在M点处SPP场可以表示为

$$E_{Mm}=\begin{cases} \left[-\cos\varphi\cos\left((a+c-1)\alpha_m+b+d\right)+\mathrm{i}\sin\varphi\sin\left((a+c-1)\alpha_m+b+d\right)\right] \\ \quad\exp\left(\mathrm{i}\left(k_{SPP}r+(-a+c)\varphi_m-b+d\right)\right),\Delta=\dfrac{\pi}{2} \\ \left[-\cos\varphi\cos\left((a+c-1)\alpha_m+b+d\right)-\mathrm{i}\sin\varphi\sin\left((a+c-1)\alpha_m+b+d\right)\right] \\ \quad\exp\left(\mathrm{i}\left(k_{SPP}r+(-a+c)\varphi_m-b+d\right)\right),\Delta=-\dfrac{\pi}{2} \end{cases} \tag{5}$$

根据文献[48]，当入射光为更特殊的圆偏光时，即$\varphi=\pi/4$时，空间任意点$q(\rho,\phi,z)$的SPP场可表示为

$$E_q=\begin{cases} r(-i)^{(2c-1)}\exp\left[\mathrm{i}\left(k_{\mathrm{SPP}}r+(2c-1)\phi+2d\right)\right]J_{2c-1}\left(k_{\mathrm{SPP}}\rho\right),\Delta=\dfrac{\pi}{2} \\ r(-i)^{(1-2a)}\exp\left[\mathrm{i}\left(k_{\mathrm{SPP}}r+(1-2a)\phi-2b\right)\right]J_{1-2a}\left(k_{\mathrm{SPP}}\rho\right),\Delta=-\dfrac{\pi}{2} \end{cases} \tag{6}$$

因此，此时PVL2被左旋圆偏光照射时，能够形成拓扑荷为$l_{\mathrm{LCP}}=2c-1$的SPP涡旋；当入射光为右旋圆偏光时，PVL2能够形成拓扑荷为$l_{\mathrm{RCP}}=1-2a$的SPP涡旋。因此，通过仅改变PVL2的结构参数a与c的值，就能够在不同旋向的圆偏光入射的情况下，形成任意拓扑荷组合的SPP涡旋场。然而当$\varphi\neq\pi/4$，即入射光为更加普通的正椭偏光时，PVL一般无法形成均匀环状分布的SPP涡旋。

然而，当满足$a+c-1=0$，$b+d=\pi/4$时，第m个组合元原子在M点处SPP场可以表示为

$$E_{Mm}=\begin{cases} \dfrac{\sqrt{2}}{2}\exp\left[\mathrm{i}\left(k_{\mathrm{SPP}}r+(1-2a)\alpha_m+2d-\varphi\right)\right],\Delta=\dfrac{\pi}{2} \\ \dfrac{\sqrt{2}}{2}\exp\left[\mathrm{i}\left(k_{\mathrm{SPP}}r+(1-2a)\alpha_m+2d+\varphi\right)\right],\Delta=-\dfrac{\pi}{2} \end{cases} \tag{7}$$

忽略SPP在传播过程中的衰减，原点附近任意一点$q(\rho,\phi,z)$处的SPP场满足：

$$E_q=\begin{cases} \dfrac{\sqrt{2}}{2}r(-\mathrm{i})^{(1-2a)}\exp\left[\mathrm{i}\left(k_{\mathrm{SPP}}r+(1-2a)\phi+2d-\varphi\right)\right]J_{1-2a}(k_{\mathrm{SPP}}\rho),\Delta=\dfrac{\pi}{2} \\ \dfrac{\sqrt{2}}{2}r(-\mathrm{i})^{(1-2a)}\exp\left[\mathrm{i}\left(k_{\mathrm{SPP}}r+(1-2a)\phi+2d+\varphi\right)\right]J_{1-2a}(k_{\mathrm{SPP}}\rho),\Delta=-\dfrac{\pi}{2} \end{cases} \tag{8}$$

从式(8)可知，类似于PVL1，无论正椭偏光的旋向和振幅比如何，最终同样都能够在PVL2的中央拓扑荷$l=1-2a$的SPP涡旋。但不同的是，入射正椭圆偏振光的旋向和振幅比信息被转移到SPP电场的相位信息中，即SPP涡旋场的强度不会随着入射正椭偏光的旋向和振幅比的改变而改变。因此，PVL2对正椭偏光旋向和振幅比不敏感。

2 结果与分析

2.1 狭缝尺寸选择

本文所有模拟均以入射光波长$\lambda=532\ \mathrm{nm}$，金的介电常数为$-4.28+\mathrm{i}1.62$为例进行，此时$\lambda_{\mathrm{SPP}}=470\ \mathrm{nm}$。在对不同PVL的功能进行验证之前，需要对组合元原子内矩形狭缝的尺寸参数进行确定。为了使矩形狭缝元原子激发的SPP场等效于一个偶极子的辐射，狭缝必须具有大的纵横比。由于组合元原子内各

个狭缝之间的间隔$D=\lambda_{SPP}/4$，因此为了避免每个组合元原子内矩形狭缝的交叉，狭缝的长度L必须小于$\lambda_{SPP}/4$。以$r_2=2\ \mu m$，$a=1.5$，$b=\pi/4$，$c=2$，$d=\pi/4$的PVL2为例进行具体说明。

图2(a)和(b)分别展示了在左旋和右旋圆偏光入射下，由$L=80\ nm$和$W=20\ nm$的狭缝组成的PVL2产生的SPP涡旋场强度与结构中心1.5 μm范围内SPP场的相位分布情况。图2(c)和(d)展示了当L不变，W变为10 nm时的PVL2产生的SPP涡旋场的强度与相位结果。对图2(a)和(b)中的强度值进行了归一化处理，其色阶标尺范围调整为0至1，同时将图2(c)和(d)的色阶标尺范围设定为与图1(a)相同的归一化比例。此外，本文所有相位结果均采用统一的色阶标尺：蓝色对应$-\pi$，渐变过渡至红色对应π。从结果可以发现，当不同旋向的圆偏光入射到两种结构上时，都形成了$l_{RCP}=-2$和$l_{LCP}=3$的SPP涡旋场，验证了一般的PVL2均能在圆偏光照射下形成拓扑荷可自由组合的SPP涡旋。并且，由尺寸为80 nm × 10 nm的狭缝组成的PVL2产生的SPP涡旋比由尺寸为80 nm × 20 nm的狭缝组成的PVL2形成的SPP涡旋场分布更均匀。这是由于矩形狭缝的尺寸效应导致激发模型与偶极子辐射模型的偏差。因此，增大矩形狭缝的长宽比可以使SPP涡旋场的分布更加均匀。然而，随着矩形狭缝的宽度从20 nm变为10 nm，SPP涡旋场的强度降低了约98%。为了权衡所形成SPP涡旋场的均匀性以及提高入射光到SPP的转换效率之间的关系，并使器件更容易加工，因此最终选择80 nm × 20 nm的矩形狭缝元原子作为构建PVL的单元结构以进行后续说明。

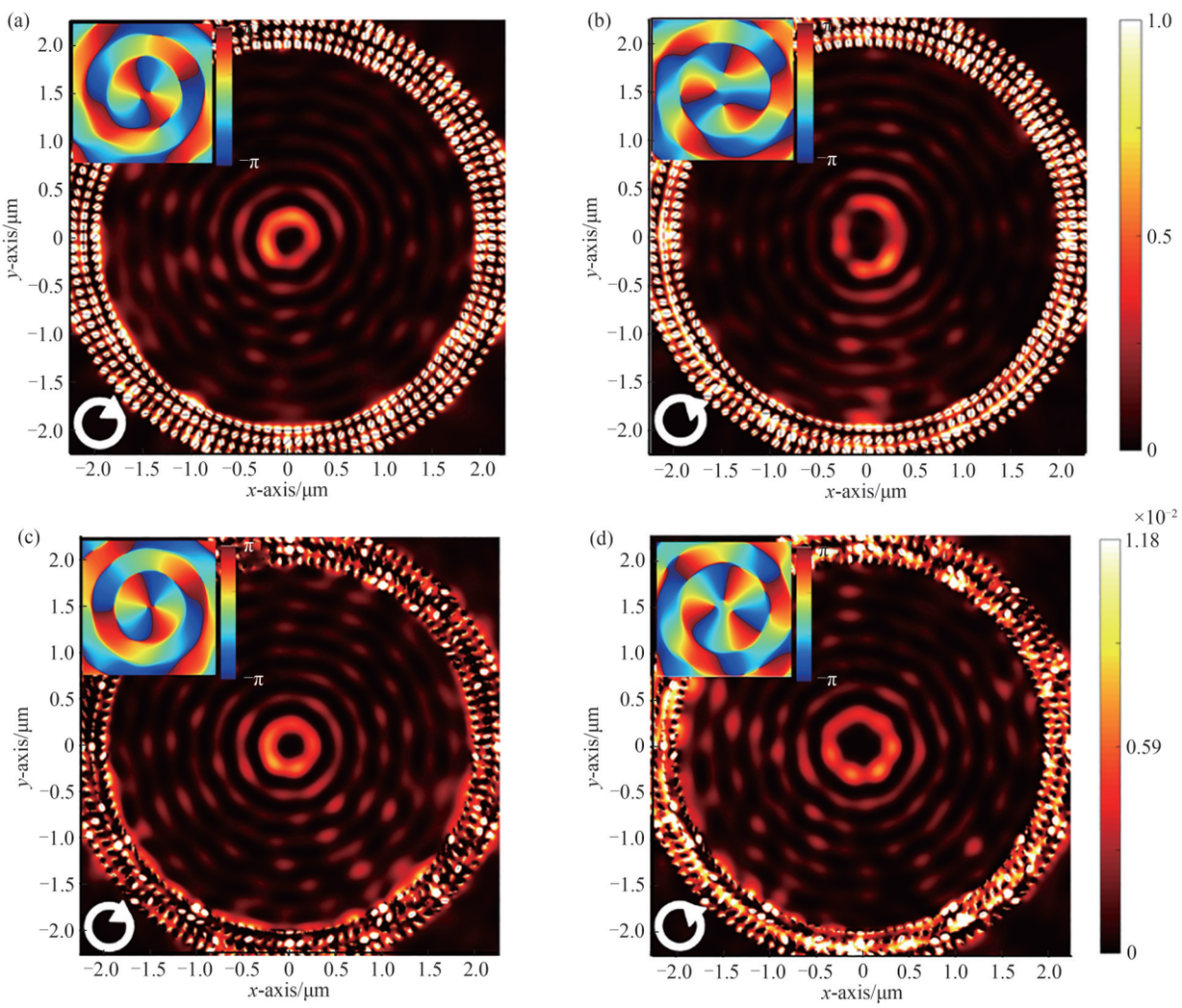


图2 不同旋向的圆偏光入射到由不同尺寸狭缝组成PVL2上时产生的SPP涡旋场强度与相位分布。(a) 80 nm × 20 nm，右旋圆偏光；(b) 80 nm × 20 nm，左旋圆偏光；(c) 80 nm × 10 nm，右旋圆偏光；(d) 80 nm × 10 nm，左旋圆偏光

Fig. 2 Intensity and phase distributions of SPP vortex fields generated by circularly polarized light with different handedness incident on the PVL2 composed of slits with different dimensions. (a) 80 nm × 20 nm, RCP; (b) 80 nm × 20 nm, LCP; (c) 80 nm × 10 nm, RCP; (d) 80 nm × 10 nm, LCP

2.2 PVL激发SPP涡旋

以a分别为0.5, 1, 1.5和2的PVL1和PVL2为例进行具体说明，将他们分别定义为PVL1-1，PVL1-2 PVL1-3，PVL1-4和PVL2-1，PVL2-2，PVL2-3以及PVL2-4。此时PVL2-1和PVL2-2满足$a+c-1=0$，$b+d=\pi/4$。表1展示出了这八个结构的参数。

表1 不同PVL1和PVL2的参数设置

Table 1 Parameters of different PVL1s and PVL2s

	PVL1-1	PVL1-2	PVL1-3	PVL1-4	PVL2-1	PVL2-2	PVL2-3	PVL2-4
a	0.5	1	1.5	2	0.5	1	1.5	2
b	$\pi/4$	$\pi/4$	$\pi/4$	$\pi/4$	$\pi/4$	$\pi/4$	$\pi/4$	$\pi/4$
c	\	\	\	\	0.5	0	−0.5	−1
d	$3\pi/4$	$3\pi/4$	$3\pi/4$	$3\pi/4$	0	0	0	0

图3展示了在$\varphi=\pi/3$的右旋正椭偏光入射下，八种不同结构形成SPP场的强度与相位分布。可以发现，$a=0.5$的PVL1和PVL2均能形成拓扑荷$l=0$的SPP实心焦点。而当a值变为1，1.5或2时，对应的PVL1和PVL2形成中心电场强度为0的环状分布SPP场。从相位分布结果发现，随着方位角逆时针增大，SPP场的相位分别经历了一次、两次和三次从π到$-\pi$的变换，据此可判定：PVL1-2和PVL2-2形成了拓扑荷$l=-1$的SPP涡旋；PVL1-3和PVL2-3形成了拓扑荷$l=-2$的SPP涡旋；PVL1-4和PVL2-4形成了拓扑荷$l=-3$的SPP涡旋。综上可知，当a相同时，PVL1和PVL2形成相同拓扑荷$l=-2a+1$的SPP聚焦涡旋场。通过调整a的取值，可改变狭缝旋转角度从而调控器件所引入的几何相位，最终实现SPP涡旋场拓扑荷的灵活调制。从图3(a)和(b)的结果比较发现，PVL1能够产生强度分布高度均匀的SPP涡旋，而PVL2所产生的SPP涡旋在均匀性上较PVL1略差。这一差异源于两者组合元原子结构的设计不同：PVL1中每个组合元原子内各矩形狭缝的之间夹角保持固定，而PVL2中各狭缝的夹角随空间角的变化而发生改变。这种构型导致PVL2所产生的SPP涡旋场具有更高的不稳定性，从而使其空间分布的均匀性有所降低。

以PVL1-4和PVL2-1为例考察PVL1和PVL2对正椭偏光的振幅比及旋向的敏感性。当不同旋向、不同振幅比(φ分别为$\pi/12$，$\pi/4$，$\pi/3$，$\pi/2$)的正椭偏光入射时，PVL1-4产生的SPP场的强度与相位分布情况

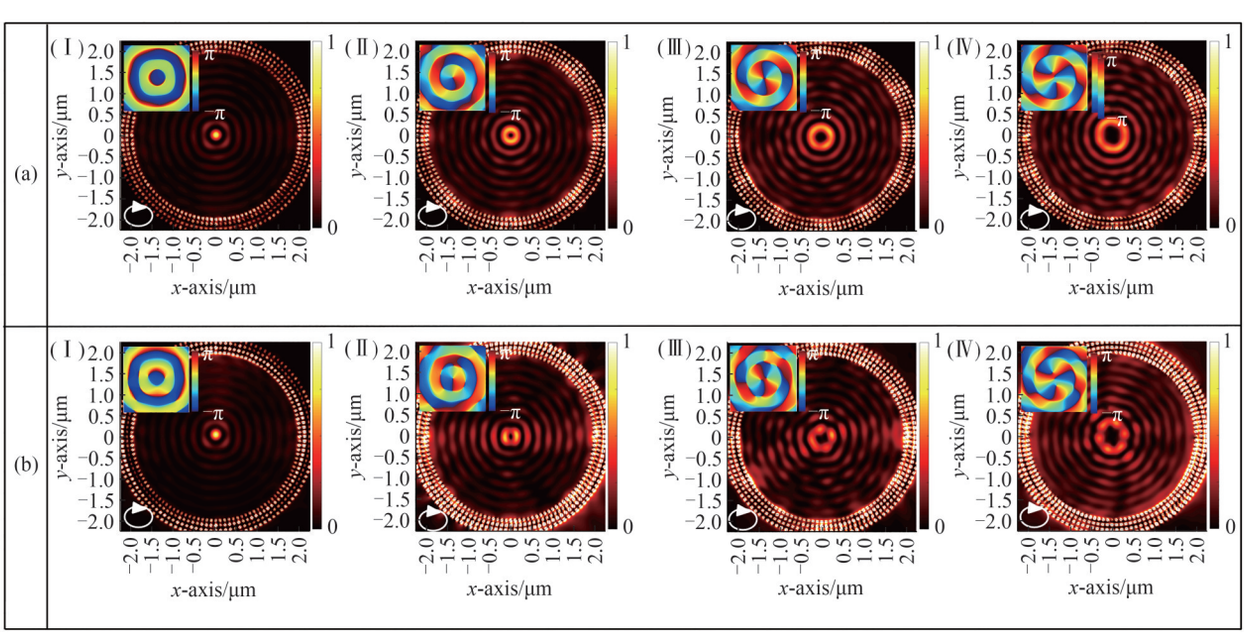


图3 具有不同a值的PVL1和PVL2在$\varphi=\pi/3$的右旋正椭偏光入射的情况下形成的SPP场的归一化强度与相位分布。(a) PVL1；(b) PVL2

Fig. 3 Intensity and phase distributions of SPP vortex fields formed by the PVL1 and PVL2 with different a under illumination with right-handed elliptically polarized light of $\varphi=\pi/3$. (a) PVL1; (b) PVL2

如图4(a)和(b)所示。结果表明,无论正椭圆偏振光的旋向和振幅比如何,均能生成拓扑荷为$l=-3$的SPP涡旋。并且,二者的变化均会导致最终SPP涡旋场的强度发生改变。式(4)表明,这是因为PVL1能将入射正椭偏光的振幅比信息φ以余弦形式调制所生成SPP涡旋场的振幅;同时,入射光旋向不同时,余弦调制间会产生$\pi/2$的相位延迟。因此,PVL1对正椭偏光的振幅比和旋向敏感。

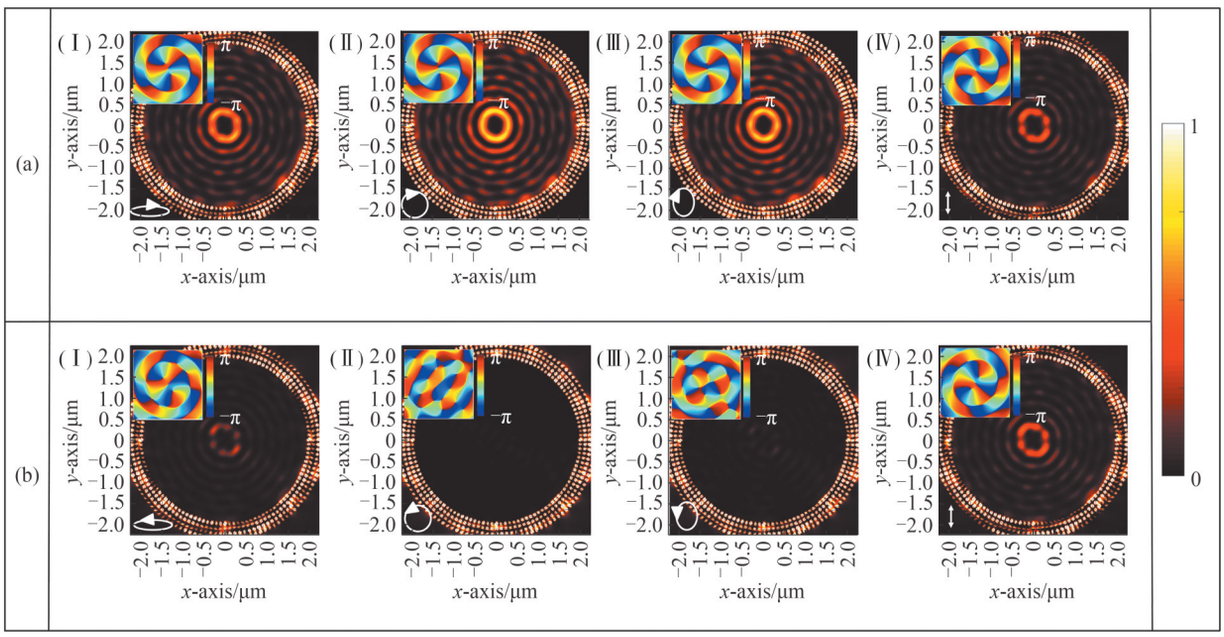


图4 不同振幅比的右旋和左旋正椭偏光照射到PVL1-4上时形成的SPP涡旋场的归一化强度与相位分布。(a)右旋正椭偏;(b)左旋正椭偏

Fig. 4 Intensity and phase distributions of SPP vortex fields formed by PVL1-4 under illumination with elliptically polarized light of varying amplitude ratios and handedness. (a) Right-handed; (b) Left-handed

从图4(a)和(b)中的Ⅱ可以看出,右旋圆偏光($\varphi=\pi/4$, $\Delta=-\pi/2$)作为一种特殊的正椭偏光入射到PVL1-4上时,所形成SPP涡旋场的强度最大;当左旋圆偏光($\varphi=\pi/4$, $\Delta=\pi/2$)入射时,PVL1-4几乎无法产生SPP涡旋。通过分别计算右旋与左旋圆偏光入射时结构中心1 μm×1 μm范围内SPP场强度密度的比值,发现这两个入射条件下所形成SPP场的强度之比超过了25,因此将右旋和左旋圆偏光入射时PVL1-4所处的状态分别定义为“开”态和“关”态,据此可将PVL1应用于光开关及圆偏光旋向检测等领域。并且,图2所示现象表明,改变矩形狭缝的长宽比可实现SPP涡旋场强度的非线性增强,这为提升开关对比度提供了新思路,即通过调控狭缝尺寸可进一步探究其对“开”、“关”态强度密度比的影响规律。

在完全相同的入射条件下,PVL2-1所激发的SPP涡旋场的强度分布与相位分布结果如图5所示。结果表明:无论入射光为左旋正椭圆偏振光或是右旋正椭圆偏振光,也无论其电场分量间的振幅比取何值,PVL2-1均能在该偏振光激发下,稳定地产生具有确定拓扑荷($l=0$)的SPP实心聚焦光斑。沿着x轴方向提取结构中心1 μm范围内$y=0$位置上SPP场的强度值,得到如图5(c)所示的归一化强度分布曲线。该曲线从数值上更加清晰的表明,SPP场的强度分布轮廓及位置,几乎不会随着入射光旋向的改变以及振幅比的调节发生变化。同时,SPP场的归一化强度峰值不仅最小值达到最大值的80%以上,其标准差也仅为0.07,故在不同偏振态正椭偏光入射下,所产生的SPP场强度可近似视为基本保持不变。而强度上的略微差异可能源于组合元原子内各狭缝产生的SPP在传播过程中受到邻近狭缝的阻碍所致。式(8)表明,SPP聚焦场强度之所以不变,是因为满足条件的PVL2能将入射正椭偏光的振幅比信息φ以及旋转方向信息转移至SPP的相位信息中。SPP焦点形态与强度分布对入射正椭圆偏振光旋向与振幅比的不依赖性,有力地验证了PVL2系列结构在正椭圆偏振光入射下,其光场调控机制与最终输出性能具有优异的偏振不敏感性。

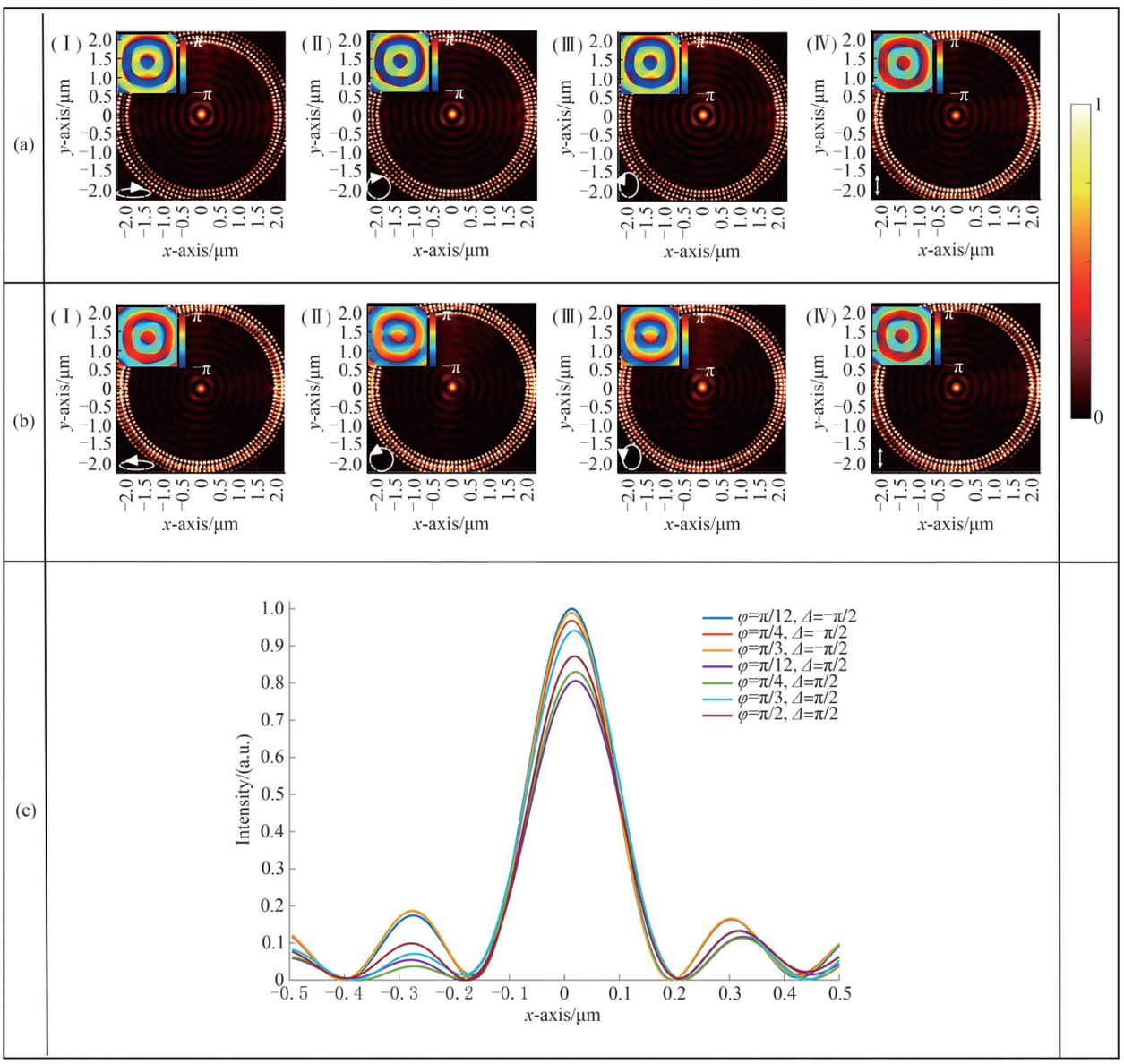


图5　不同振幅比的右旋和左旋正椭偏光照射到PVL2-1上时形成的SPP涡旋场的归一化强度与相位分布情况。(a)右旋正椭偏；(b)左旋正椭偏；(c)图(a)与图(b)中沿y=0位置的x轴方向强度分布

Fig. 5　Intensity and phase distributions of SPP vortex fields formed by PVL2-1 under illumination with elliptically polarized light of varying amplitude ratios and handedness. (a) Right-handed; (b) Left-handed; (c) The intensity distribution along the x-axis for y = 0 of (a) and (b)

3　结论

本文提出了一种由四个矩形狭缝构成的元原子组成的PVL。通过调整元原子内矩形狭缝的旋转角度，形成了两种利用正椭偏光作为激励源且仅基于几何相位设计的PVL，其中一种为对入射的正椭偏光的旋向和振幅比敏感的PVL1，另一种则为对入射的正椭偏光的旋向和振幅比不敏感的PVL2。在此基础上，通过调整矩形狭缝的旋转角度，能够调整PVL所形成SPP涡旋场的拓扑荷。利用这些特性，可以将这两种PVL应用于光镊、光场调制、光开关等领域，因此这项工作拓展了PVL的应用领域与应用场景。此外，由于器件仅使用单一形状和尺寸的狭缝结构且未引入传输相位，所以这在器件设计流程的简易化、器件的小型化等方面具有优势，有助于光子器件的设计与集成化应用。

参考文献

[1]　GONG T, LUO Y, ZHAO C, et al. Highly reproducible and stable surface-enhanced Raman scattering substrates of

graphene-Ag nanohole arrays fabricated by sub-diffraction plasmonic lithography[J]. OSA Continuum, 2019, 2(3): 582-594.
[2] HU Y, LI L, WANG R, et al. High-speed parallel plasmonic direct-writing nanolithography using metasurface-based plasmonic lens[J]. Engineering, 2021, 7(11): 1623-1630.
[3] TAN H M, PECHPRASARN S, ZHANG J, et al. High resolution quantitative angle-scanning widefield surface plasmon microscopy[J]. Scientific Reports, 2016, 6(1): 20195.
[4] CAO Y, YANG S, WANG D, et al. Surface plasmon-enhanced dark-field microsphere-assisted microscopy[J]. Optics Express, 2023, 31(5): 8641-8649.
[5] AZAD Z, TALUKDER M A. Simultaneously surface-and edge-emitting plasmonic laser operating in the near-infrared region[J]. Optics & Laser Technology, 2022, 146(1): 107571.
[6] BOZHEVOLNYI S I, KHURGIN J B. Fundamental limitations in spontaneous emission rate of single-photon sources[J]. Optica, 2016, 3(12): 1418-1421.
[7] WU C, KUMAR S, KAN Y, et al. Room-temperature on-chip orbital angular momentum single-photon sources[J]. Science Advances, 2022, 8(2): eabk3075.
[8] DEY A, PRAMANIK A, MONDAL K, et al. Emission peak shifted incoherent random laser through the combined effects of coupling of surface plasmons in a triangular shaped silver nanostructure, microbubbles, and the waveguiding mechanism[J]. Journal of the Optical Society of America B, 2023, 40(5): 1039-1046.
[9] KAN Y, KUMAR S, DING F, et al. Spin-orbit controlled excitation of quantum emitters in hybrid plasmonic nanocircuits[J]. Advanced Optical Materials, 2020, 8(21):2000854.
[10] PORS A, BOZHEVOLNYI S I. Quantum emitters near layered plasmonic nanostructures: decay rate contributions[J]. ACS Photonics, 2015, 2(2): 228-236.
[11] SIAMPOUR H, KUMAR S, DAVYDOV V A, et al. On-chip excitation of single germanium vacancies in nanodiamonds embedded in plasmonic waveguides[J]. Light-Science & Applications, 2018, 7(1): 61.
[12] CHEN J, CHENG L, ZHAO L, et al. Surface plasmon polaritons enhanced magnetic plasmon resonance for high-quality sensing[J]. Applied Physics Express, 2022, 15(12): 122008.
[13] DE ANGELIS F, DAS G, CANDELORO P, et al. Nanoscale chemical mapping using three-dimensional adiabatic compression of surface plasmon polaritons[J]. Nature Nanotechnology, 2010, 5(1): 67-72.
[14] HOMOLA J. Present and future of surface plasmon resonance biosensors[J]. Analytical and Bioanalytical Chemistry, 2003, 377(3): 528-539.
[15] PENG Y, HUANG J, LUO J, et al. Three-step one-way model in terahertz biomedical detection[J]. PhotoniX, 2021, 2(1): 12.
[16] TENE T, GUEVARA M, SVOZILIK J, et al. Proving surface plasmons in graphene nanoribbons organized as 2D periodic arrays and potential applications in biosensors[J]. Chemosensors, 2022, 10(12): 514.
[17] LIU Y, PENG W. Fiber-optic surface plasmon resonance sensors and biochemical applications: a review[J]. Journal of Lightwave Technology, 2020, 39(12): 3781-3791.
[18] LI Z, WU X, TONG K, et al. Sucrose concentration sensor based on MoS_2 nanofilm and Au nanowire array enhanced surface plasmon resonance with a graphene oxide nanosheet[J]. Journal of Optical Technology, 2020, 87(1): 40-44.
[19] RAHAMAN M, MILEKHIN A G, MUKHERJEE A, et al. The role of a plasmonic substrate on the enhancement and spatial resolution of tip-enhanced Raman scattering[J]. Faraday Discussions, 2019, 214: 309-323.
[20] ZHOU Y, LU Y, LIU Y, et al. Current strategies of plasmonic nanoparticles assisted surface-enhanced Raman scattering toward biosensor studies[J]. Biosensors & Bioelectronics, 2023, 228(32): 115231.
[21] ZHANG L, MENG C, YANG H, et al. Azimuthal vector beam illuminating plasmonic tips circular cluster for surface-enhanced Raman spectroscopy[J]. Chinese Optics Letters, 2023, 21(3): 033603.
[22] DEVAUX E, EBBESEN T W, WEEBER J C, et al. Launching and decoupling surface plasmons via micro-gratings[J]. Applied Physics Letters, 2003, 83(24): 4936-4938.
[23] GENEVET P, YU N, AIETA F, et al. Ultra-thin plasmonic optical vortex plate based on phase discontinuities[J]. Applied Physics Letters, 2012, 100(1): 013101.
[24] TSAI W Y, HUANG J S, HUANG C B, Selective trapping or rotation of isotropic dielectric microparticles by optical near field in a plasmonic archimedes spiral[J]. Nano Letters, 2014, 14(2): 547 - 552.
[25] GU K, ZHAO H, SUN M, et al. A feasibility study on scanning imaging of tip-enhanced raman spectroscopy using a spiral plasmonic lens[J]. Optical and Quantum Electron, 2024, 56(7): 1274.
[26] GU K, SUN M, ZHANG Y. Tip-enhanced Raman spectroscopy based on spiral plasmonic lens excitation[J]. Sensors, 2022, 22(15): 5636.
[27] CHEN J, CHEN X, LI T, et al. On-chip detection of orbital angular momentum beam by plasmonic nanogratings[J]. Laser Photonics Review, 2018, 12(8): 1700331.
[28] FANG X, REN H, GU M. Orbital angular momentum holography for high-security encryption[J]. Nature Photonics,

2020, 14(2): 102-108.
[29] CHEN W, NELSON R L, ZHAN Q. Geometrical phase and surface plasmon focusing with azimuthal polarization[J]. Optics Letters, 2012, 37(4): 581-583.
[30] CHEN C, KU C, TAI Y, et al. Creating optical near-field orbital angular momentum in a gold metasurface[J]. Nano Letters, 2015, 15(4): 2746-2750.
[31] XU Q, MA S, HU C, et al. Coupling-mediated selective spin-to-plasmonic-orbital angular momentum conversion[J]. Advanced Optical Materials, 2019, 7(20): 035802.
[32] JIN Z, JANOSCHKA D, DENG J, et al. Phyllotaxis-inspired nanosieves with multiplexed orbital angular momentum [J]. eLight, 2021, 1(5): 1-11.
[33] LEE S, KIM S, KWON H, et al. Spin-direction control of high-order plasmonic vortex with double-ring distributed nanoslits[J]. IEEE Photonics Technology Letters, 2015, 27(7): 705-708.
[34] LI J, TANG P, LIU W, et al. Plasmonic circular polarization analyzer formed by unidirectionally controlling surface plasmon propagation[J]. Applied Physics Letters, 2015, 106(16): 161106.
[35] HUANG F, JIANG X, YUAN H, et al. Generation of plasmonic vortex with linearly polarized light[J]. Plasmonics, 2017, 12(3): 751-757.
[36] MOON S W, JEONG H, LEE S, et al. Compensation of spin-orbit interaction using the geometric phase of distributed nanoslits for polarization-independent plasmonic vortex generation[J]. Optics Express, 2019, 27(14): 19119-19129.
[37] MOON S W, LEE S Y. Ultracompact plasmonic meta-pixel for arbitrary polarization detection[J]. Plasmonics, 2020, 15(6): 1781-1788.
[38] TANG B, ZHANG B, DING J. Generating a plasmonic vortex field with arbitrary topological charges and positions by meta-nanoslits[J]. Applied Optics, 2019, 58(4): 833-840.
[39] GU K, ZHANG Y, ZHAO H, et al., Manipulation of plasmonic vortex fields using positive elliptically polarized beams [J]. Optics & Laser Technology. 2024, 169(1): 110132.
[40] TSAI W Y, HUANG J S, HUANG C B. Selective trapping or rotation of isotropic dielectric microparticles by optical near field in a plasmonic Archimedes spiral[J]. Nano Letters, 2014, 14(2): 547-552.
[41] FARRÉ A, HORST A, BLAB G A, et al. Stretching single DNA molecules to demonstrate high-force capabilities of holographic optical tweezers[J]. Journal of Biophotonics, 2010, 3(4): 224-233.
[42] LALANNE P, HUGONIN J P, RODIER J C. Approximate model for surface-plasmon generation at slit apertures[J]. Journal of the Optical Society of America A, 2006, 23(7): 1608-1615.
[43] LALANNE P, HUGONIN J, RODIER J. Theory of surface plasmon generation at nanoslit apertures [J]. Physical Review Letters, 2005, 95(26): 263902.
[44] CHANG S H, GRAY S K, SCHATZ G C. Surface plasmon generation and light transmission by isolated nanoholes and arrays of nanoholes in thin metal films[J]. Optics Express, 2005, 13(8): 3150-3165.
[45] LIN J, MUELLER J P B, WANG Q, et al. Polarization-controlled tunable directional coupling of surface plasmon polaritons[J]. Science, 2013, 340(6130): 331-334.
[46] MOU Z, ZHOU C, LV H, et al. Uniform theory of plasmonic vortex generation based on nanoholes [J]. Nanotechnology, 2020, 31(45): 455301.
[47] TAN C Z. Angular momentum and the Stokes parameters of an elliptically polarized electromagnetic wave[J]. Optik, 2017, 134: 280-286.
[48] GU K, ZHANG Y, ZHAO H, et al. Manipulating plasmonic vortex based on meta-atoms with four rectangular slits[J]. Optics Express, 2023, 31(24): 39927-39940.

Manipulation of Surface Plasmon Polariton Vortices via Positive Elliptically Polarized Light and Geometric Phase

GU Kai, SUN Fanxi, TAO Guanyu
(*School of Mathematics and Physics*, *Suqian University*, *Suqian* 223800, *China*)

Abstract: The Surface Plasmon Polariton (SPP) vortices confined to a metal-dielectric interface, are characterized by the near-field enhancement and orbital angular momentum. They find broad applications in particle manipulation, super-resolution imaging, biochemical sensing, and so on. Recent advances in Plasmonic Vortex Lenses (PVLs) for SPP vortex generation have progressively simplified the excitation

source requirements—evolving from complex vector beams inherently carrying orbital angular momentum to scalar fields employing circularly or linearly polarized light. Although positive elliptically polarized light, as a fundamental polarization state of scalar fields, has been utilized for PVL excitation, the existing schemes necessitate the incorporation of additional transmission phases—achieved through spiral contour designs—to generate arbitrary-order SPP vortices under positive elliptically polarized light. The SPPs generated by the meta-atoms arranged at the end of the spiral have more attenuation because of the more optical paths they have to travel than those generated by the slit pairs at the front, which ultimately leads to an uneven field distribution of the SPP vortex. Furthermore, an issue arises as the size of the PVL increases with the radius of the spiral contour, presenting a challenge for miniaturizing the PVLs. Furthermore, these devices exhibit inherent polarization sensitivity, which substantially restricts the application scenarios of both SPP vortices and PVLs.

To address the aforementioned challenges, this work proposes a geometric phase-based PVL. The lens comprises composite meta-atoms arranged along a circular contour, with each meta-atom integrating four rectangular slits. By systematically controlling the rotation angles of slits within meta-atoms, the proposed PVL not only generates SPP vortices sensitive or insensitive to the amplitude ratio and handedness of incident positive elliptically polarized light but also enables flexible manipulation of the Topological Charge (TC) of the SPP vortices. Specifically, the rotation angles of slits are adjusted through four parameters, namely a, b, c, and d, to construct different configurations of PVL1 and PVL2. Under illumination by the positive elliptically polarized light of arbitrary handedness and amplitude ratio, PVL1 generates SPP vortices with a TC of $l=1-2a$, and the intensity of the vortex field varies with changes in the incident light's handedness and amplitude ratio. When illuminated by circularly polarized light of opposite handedness, PVL2 produces SPP vortices with TCs of $l_{\mathrm{LCP}}=2c-1$ and $l_{\mathrm{RCP}}=1-2a$. Notably, under the condition $a+c-1=0$ and $b+d=\pi/4$, PVL2 generates SPP vortices with $l=1-2a$ for any positive elliptically polarized incident light, and the vortex field intensity remains invariant to changes in the incident polarization's handedness or amplitude ratio. By modulating the slit rotation parameter a, the TC of SPP vortices generated by both PVL1 and PVL2 can be tuned. To demonstrate the properties of PVL1 and PVL2, eight structures with a of 0.5, 1, 1.5 and 2 respectively were designed. Finite-difference Time-domain (FDTD) simulations reveal that PVL1-1 and PVL2-1 both generate SPP focal spots with $l=0$. When a is 1, 1.5 and 2 respectively, both PVL1 and PVL2 produce SPP vortices with TC of -1, -2 and -3 respectively. Crucially, the intensity of the SPP field generated by PVL1 varies with the amplitude ratio and handedness of the incident positive elliptically polarized light, confirming its polarization-sensitive nature. In contrast, the SPP field intensity from PVL2 remains unchanged under identical variations, validating its polarization-insensitive functionality.

Leveraging these functionalities, the proposed PVLs can be deployed in optical tweezers, optical field manipulation, and optical switching systems, thereby expanding the application domains and practical scenarios for plasmonic vortex lenses. Beyond this extended applicability, the device architecture offers inherent advantages in simplified fabrication workflows and miniaturization. This stems from its exclusive use of single-shaped, uniformly sized slit structures and the absence of introduced transmission phases. These features collectively facilitate the streamlined design and on-chip integration of advanced photonic devices.

Key words: Surface plasmon polariton; Vortices; Topological charge; Positive elliptically polarized light; Geometric phase; Polarization sensitivity

OCIS Codes: 240.6680; 240.3990; 240.5420

CSTR: 32255.14.gzxb20265501.0124001

Foundation item: Suqian Sci&Tech Program (K202536), Suqian University Research Start-up Fund for Talent Introduction (2025XRC006)